

Global Distribution of Ionizing and Recombining Plasmas in the Supernova Remnant G290.1—0.8

Fumiyoshi KAMITSUKASA,¹ Katsuji KOYAMA,^{1,2} Hiroyuki UCHIDA,² Hiroshi NAKAJIMA,¹
Kiyoshi HAYASHIDA,¹ Koji MORI,³ Satoru KATSUDA,⁴ and Hiroshi TSUNEMI,¹

¹*Department of Earth and Space Science, Osaka University, 1-1 Machikaneyama-cho, Toyonaka, Osaka
560-0043, Japan*

²*Department of Physics, Graduate School of Science, Kyoto University, Kitashirakawa Oiwake-cho, Sakyo-ku,
Kyoto 606-8502, Japan*

³*Department of Applied Physics and Electronic Engineering, Faculty of Engineering, University of Miyazaki,
1-1 Gakuen Kibanadai-Nishi, Miyazaki 889-2192, Japan*

⁴*Institute of Space and Astronautical Science, 3-1-1, Yoshinodai, Sagamihara, Kanagawa 229-8510, Japan
kamitsukasa@ess.sci.osaka-u.ac.jp*

(Received 2014 September 30; accepted 2014 November 25)

Abstract

We report on the Suzaku results of the mixed-morphology supernova remnant (SNR) G290.1—0.8 (MSH 11-61A). The SNR has an asymmetric structure extended to the south-east and the northwest. In the X-ray spectra of the center and the northwest regions, we discover recombining plasma features with the strong Si Ly α and radiative recombination continuum at ~ 2.7 keV. These features are the most significant in the northwest region, and the spectra are well-reproduced with a recombining plasma of $kT_e = 0.5$ keV. Whereas the spectra of other regions are expressed by an ionizing plasma of $kT_e = 0.6$ keV. The recombining plasma has over-solar abundances, while the ionizing plasma has roughly solar abundances. Hence they are likely ejecta and interstellar medium (ISM) origin, respectively. The recombining plasma in the northwest of G290.1—0.8 would be generated by a break-out of the supernova ejecta from a high density circumstellar medium to a low density ISM.

Key words: ISM: abundances — ISM: individual (G290.1—0.8) — ISM: supernova remnants — X-rays: ISM

1. Introduction

A quarter of the X-ray-detected supernova remnants (SNRs) in our Galaxy belong to a mixed-morphology (MM) SNR (Jones et al. 1998). They have center-filled thermal X-ray emissions in a

synchrotron radio shell (Rho & Petre 1998). They are generally associated with molecular clouds, and often contain OH (1720 MHz) masers (e.g., Yusef-Zadeh et al. 2003). Some MM SNRs exhibit the TeV/GeV gamma-ray emissions, indicating the presence of high energy protons interacting with molecular clouds (e.g., Abdo et al. 2010). These facts suggest that MM SNRs are located in the dense environments which contain massive stars. Therefore, we expect that they are originated in core-collapse supernovae (CC SNe).

Recently, the Suzaku satellite has discovered strong radiative recombination continua (RRC) in the X-ray spectra of several MM SNRs (e.g., W49B: Ozawa et al. 2009; IC 443: Yamaguchi et al. 2009, Ohnishi et al. 2014; G359.1–0.5: Ohnishi et al. 2011; W28: Sawada & Koyama 2012; W44: Uchida et al. 2012; G346.6–0.2: Yamauchi et al. 2013; 3C 391: Ergin et al. 2014). In the case of W49B, with the XMM-Newton, Miceli et al. (2010) confirmed the RRC feature and found that it is spatially localized. The strong RRC emissions are the direct evidence that these SNRs have recombining plasmas (RPs). The RP is also characterized with a higher ionization temperature, kT_z , than an electron temperature, kT_e , unlike a collisional ionization equilibrium (CIE: $kT_e = kT_z$) or an ionizing plasma (IP: $kT_e > kT_z$). Although the formation process of the RP has not been understood yet, the strong correlation between the RPs and the MM SNRs suggests that the RP would be formed under the environments for MM SNRs.

Kesteven (1968) discovered G290.1–0.8, also known as MSH 11-61A, in the radio band. The radio image obtained with the Molonglo Observation Synthesis Telescope (MOST) revealed its asymmetric geometry elongated in the southeast and the northwest direction with the size of $15' \times 10'$ (Kesteven & Caswell 1987; Milne et al. 1989). Filipovic et al. (2005) reported that the NANTEN CO data suggest a dense molecular cloud in the southeast of the SNR. Reynoso et al. (2006) studied the gas distribution and kinematics in detail, and suggested that the SNR probably lies in the Carina arm, at a distance of 7 ± 1 kpc.

In X-ray, G290.1–0.8 was found by the Galactic SNRs survey with the Einstein Observatory (Seward 1990). The Advanced Satellite for Cosmology and Astrophysics (ASCA) found that the X-ray is a thermal plasma emission, and then classified this SNR as a member of the MM SNRs (Rho & Petre 1998). García et al. (2012) analyzed the XMM-Newton and the Chandra data focusing on the asymmetric geometry of the SNR. They concluded that the plasmas in the southeast and the northwest regions are IPs, while those in the other regions are CIEs. Employing these X-ray results and the H_I map, they proposed that the SNR is due to a core collapse of a high mass progenitor with a bipolar wind.

Pavan et al. (2011) discovered a hard X-ray source, IGR J11014-6103, about $10'$ at the southwest of G290.1–0.8. Halpern et al. (2014) detected the pulsation of 62.8 msec. This pulsar has a prominent jet extending toward the northwest and a possible counter jet to the southeast (Pavan et al. 2014). It also has a bow shock tail pointing to the center of G290.1–0.8. Moreover, the absorption (N_H) of the pulsar is similar to that of G290.1–0.8. Thus IGR J11014-6103 would be an associated pulsar of G290.1–0.8, a compact remnant of a CC SN. Halpern et al. (2014) estimated the spin-down

age to be 116 kyr, significantly larger than the previous estimation of the SNR age of 10–20 kyr (Slane et al. 2002).

In this paper, we present the Suzaku observation results of G290.1–0.8. The size of the SNR allows us to perform a spatially resolved spectroscopic study by using the Suzaku telescope. The high sensitivity and the high energy resolution of Suzaku enable us to accurately determine the X-ray spectral features of the thermal plasma. We report the first discovery of the RP from this SNR. Based on the detailed analysis of the plasma structure, we discuss the evolution of G290.1–0.8.

2. Observation and Data Reduction

The Suzaku satellite (Mitsuda et al. 2007) observed G290.1–0.8 on 2011 June 25 (PI: K. Koyama) with the X-ray Imaging Spectrometer (XIS; Koyama et al. 2007). The observation log is given in table 1. The XIS consists of three active sensors placed on the focal planes of the X-ray Telescopes (XRTs; Serlemitsos et al. 2007). Two of the XIS are front-illuminated (FI) CCDs, sensitive in the 0.4–14 keV, while the other is a back-illuminated (BI) CCD, with high sensitivity down to 0.2 keV. The spaced-row charge injection (SCI; Nakajima et al. 2008) technique was performed for all of the XIS on this observation. We use the version 6.15 of the HEASoft tools (ver.19 of the Suzaku software) for the data reduction. The archival data are reprocessed with the calibration data base (CALDB) released in 2014 April. The total exposure time after the standard screening¹ is about 110 ks.

3. Analyses and Results

3.1. Imaging Analysis

Figure 1 shows X-ray images in the 0.6–1.5 and 1.5–4 keV bands. We combine the data from all the XIS to maximize the photon statistics. The images are binned with $2''1 \times 2''1$ and smoothed with a Gaussian kernel of $\sigma = 0''.5$. We overlay the 843 MHz radio profile obtained by the MOST with white contours. We can see a center-filled X-ray emission in the radio shell, which is the typical feature of the MM SNRs. The diffuse emission from G290.1–0.8 is mainly found in the 0.6–4 keV band; no significant emission except the X-ray background is found above this energy band. We see ear-like structures at the southeast and the northwest that are prominent in the 1.5–4 keV band.

3.2. Spectral Analysis

We use the XSPEC software version 12.8.2a in the following analysis. The redistribution matrix files (RMFs) and the ancillary response files (ARFs) are generated with `xisrmfgen` and `xisarfgen` (Ishisaki et al. 2007), respectively. We adopt the solar abundances of Anders & Grevesse (1989). Unless otherwise specified, all errors represent 90 % confidence levels.

¹ http://heasarc.nasa.gov/docs/suzaku/processing/criteria_xis.html

3.2.1. Background Estimation

Since G290.1–0.8 extends widely over the field of view (FoV) of the XIS, the X-ray background region is not available from the same FoV. Therefore, we use the data from a nearby sky field: a blank region in the field of the X-ray pulsar 1E1048.1–5937. We extract the background data from the whole FoV of the XIS, excluding the pulsar region of $4'$ radius. We generate the non X-ray background (NXB) using `xisnxbgen` (Tawa et al. 2008) and subtract it from the extracted spectrum. This background spectrum consists of the cosmic X-ray background (CXB), the Galactic ridge X-ray emission (GRXE), and the Galactic halo (GH) (e.g., Kushino et al. 2002; Kaneda et al. 1997; Henley & Shelton 2013). Then, we fit the spectrum with a model of $[\text{Abs1} \times \text{powerlaw (CXB)} + \text{Abs2} \times (\text{apec (HP)} + \text{apec (LP)}) + \text{Abs3} \times \text{apec (GH)}]$, where the `apec` is a CIE plasma model in the XSPEC. The second term is the GRXE component, which is represented with a 2-CIE model, a high-temperature plasma (HP; $kT_e \sim 7$ keV) + a low-temperature plasma (LP; $kT_e \sim 1$ keV) (Kaneda et al. 1997; Uchiyama et al. 2013). The CXB component parameters are fixed at those in Kushino et al. (2002). The model is nicely fitted with $\chi^2_{\nu}/\text{d.o.f.} = 1.08/1111$, where χ^2_{ν} and d.o.f. represent the reduced chi square and the degree of freedom. The best-fit parameters are given in the table 2.

Since the Galactic coordinate of G290.1–0.8 is slightly different from that of the 1E1048.1–5937 field, we fine-tune the GRXE flux using the spatial structure of the GRXE. Kaneda et al. (1997) estimated its Galactic latitude distribution by an exponential function with the e-folding values of $\sim 0.5^\circ$ and 1° for the HP and the LP, respectively. Uchiyama et al. (2013) estimated the Galactic longitude distribution by an exponential function with the e-folding values of $\sim 50^\circ$ both for the HP and the LP. Then, we can estimate the fluxes of the HP and the LP at G290.1–0.8 to be $\sim 60\%$ and $\sim 80\%$ of those at 1E1048.1–5937 field.

3.2.2. Analyses of the Spectra

Since the spatial structure of G290.1–0.8 is asymmetric (Kesteven & Caswell 1987), we divide the SNR into the Center, NW, SE, NE, and SW regions as shown in figure 1 (b). The NXB-subtracted spectra are shown in figure 2. We first apply a 1-component IP adding the background model spectrum given in the previous subsection. We use the plasma code (`vvrnei`) in the XSPEC package. The `vvrnei` calculates the spectrum of a non-equilibrium ionization plasma after a rapid transition of the electron temperature from kT_{init} to kT_e . The initial plasma temperature kT_{init} is fixed at 0.01 keV. The present electron temperature kT_e , ionization timescale $n_e t$, emission measure, and column density N_H are free parameters, where n_e and t are an electron density and an elapsed time after the initial state. The abundances of Ne, Mg, Si, S, Ar, and Fe are also allowed to vary freely, while the abundances of Ca and Ni are linked to those of Ar and Fe, respectively. The CXB flux is free within the fluctuation expected for the area of each region (Kushino et al. 2002), while the other background parameters are fixed to the values in the table 2.

This fit, however, leaves a large residual around 1.2 keV. This residual is due to the error of Fe-L lines in the current XSPEC code (e.g., Borkowski et al. 2006; Yamaguchi et al. 2011). We therefore add a Gaussian line at 1.2 keV. The χ^2_{ν} values are improved to 1.19 (Center), 1.24 (NW), 1.08 (SE),

1.06 (NE), and 1.10 (SW). Contrary to the nice fits for the SE, NE and SW regions, the IP models for the Center and particularly the NW spectra are rejected with the large χ^2_ν values. For example, the fits of the NW spectra leave hump-like residuals around 2.7 keV and line-like residuals at 2.0 keV (see the middle panels of the NW spectra in figure 2). The former residuals correspond to the RRC of Si, while the latter are Si Ly α (2.01 keV). These residuals indicate that the ionization state of Si is higher than that expected from the IP model. In particular, the RRC structure of Si strongly suggests that the plasma is in a recombining phase.

We therefore apply RP models for the spectra of the Center and the NW (1-component RP plus a Gaussian line). Unlike the fixed initial temperature kT_{init} of 0.01 keV in the IP fit, the RP fit assumes a high temperature in the initial phase of the plasma. The RP fit assumes a rapid electron cooling of $kT_{\text{init}} \rightarrow kT_e$ at an early phase of the plasma evolution. Thus the free parameters are kT_{init} , kT_e , and $n_e t$, where t is an elapsed time after the rapid cooling of the electron temperature. This RP model fit significantly improves the χ^2_ν value to 1.12 and 1.10 for the Center and the NW spectra, respectively. The hump-like residuals in the IP fits disappear in the RP fits (see the bottom panels of the Center and NW spectra in figure 2). On the other hand, the RP fits for the SE, NE and SW spectra do not significantly improve the χ^2_ν value from those of the IP fits. Although the hump-like residuals also seen in the NE, the current photon statistics does not allow us to discriminate the IP and RP models.

The best-fit spectra and parameters for the RP fits (Center and NW) and IP fits (SE, NE, and SW) are shown in the figure 2 and table 3. The null hypothesis probabilities of the IP fits are 8×10^{-7} (Center), 9×10^{-6} (NW), 0.03 (SE), 0.08 (NE), and 0.01 (SW), while those of the RP fits are 0.001 (Center), 0.03 (NW). Although all the spectra are statistically rejected under the canonical criterion of the null probability of 0.1, the IP fits for the SE, NE and SW and the RP fits for the Center and NW are marginally acceptable by taking account of possible systematic errors.

We select the similar regions to those employed in García et al. (2012). They reported that CIE models adequately describe some of the regions. We therefore try CIE models for the direct comparison between the Suzaku and the XMM-Newton results. The CIE results, however, show no significant difference from the IP fits within the systematical uncertainty; the χ^2_ν values of the CIE fits are 1.22 (Center), 1.24 (NW), 1.12 (SE), 1.09 (NE), and 1.11 (SW). We thus use the IP fit results for the SE, NE, and SW regions, while the RP results for the Center and NW regions in the following discussion as the good approximation.

4. Discussion

We find that the spectrum of G290.1–0.8 is well described by RPs in the Center and NW regions, while those in the SE, NE and SW regions are IPs. The electron temperatures are $0.45^{+0.02}_{-0.01}$ keV (Center), $0.52^{+0.02}_{-0.04}$ keV (NW), $0.66^{+0.03}_{-0.02}$ keV (SE), $0.64^{+0.02}_{-0.01}$ keV (NE), and $0.59^{+0.03}_{-0.02}$ keV (SW). Thus the temperatures of the RP regions (Center and NW) are lower than those of the IP regions (SE, NE, and SW) about 25 %. The ionization parameter ($n_e t$) in the NW region is

smaller than that in the Center region, which is consistent with the fact that the apparent RRC feature in the NW spectrum is clearer than that in the Center. In contrast, the XMM-Newton observations reported the plasma of IP or CIE in all the regions (García et al. 2012). We believe that the discrepancy is due to the better energy resolution and photon statistics in the hard energy band of Suzaku than those of XMM-Newton (as in the case of IC 443; Yamaguchi et al. 2009).

As we noted in the section 3.2.2, we allowed the possible fluctuation of the CXB in the source regions. We here examine the effect of the CXB fluctuation changing the flux by $\pm 50\%$, which is the largest deviation expected for each region, of the nominal value (Kushino et al. 2002). The results, however, show no significant change of the χ^2_ν and the best-fit parameters; for example the electron temperatures change only by 0.01 keV, which is within the range of the statistical errors.

The abundances of the RP are over-solar, while those of the IP except in the SE region are roughly 1 solar. The abundances in the SE region seem intermediate between those in the RP and IP regions. Probably, the plasma in the SE region is a mixture of the RP and the IP. In fact, although the significance level is low, the RP fit for the SE ($\chi^2/\text{d.o.f.} = 1210/1125$) is slightly better than the pure IP fit ($\chi^2/\text{d.o.f.} = 1215/1126$).

The abundance pattern of the RP in NW is shown in figure 3 together with the prediction from the massive progenitor (Woosley & Weaver 1995). The pattern is roughly similar to that of ejecta from the progenitor star of $M = 20\text{--}25 M_\odot$. On the other hand, the solar abundances of the IP in the NE and SW regions suggest that the plasma is ISM origin.

In detail, the Ne and Fe abundances in every region are systematically lower than the other elements. The Fe abundances are mainly determined by the line fluxes of Fe-L lines, which have rather large uncertainty in the present plasma code. The main transitions are $3s \rightarrow 2p$ (~ 0.7 keV) and $3d \rightarrow 2p$ (~ 0.8 keV) of Fe XVII. These low energy line fluxes are significantly affected by the low energy absorptions and contamination from the $\text{Ly}\beta$ of O VIII (0.77 keV). As the results, the Fe abundance may have a large error, and hence apparent depletion of Fe may occur. The Ne abundances are due to $K\alpha$ lines of Ne IX and Ne X. The L-line energies from more highly ionized Fe XIX come near the $K\alpha$ of Ne IX (e.g., see Brinkman et al. 2000). Therefore, coupled to the large error of Fe abundance, the Ne abundance would have a large error too. However, the reason of apparent Ne depletion is somehow puzzling. We simply note that the same depletions of Ne and Fe are observed in García et al. (2012), and also reported from other SNRs (e.g., W28, Sawada & Koyama 2012).

To form the RP in the Center and the NW regions, either a rapid electron cooling or an enhancement of ionization should occur. In the former case, the electron temperature is expected to be lower in the RP region, while visa versa for the latter case. Since our results show a lower temperature of the RP than that of the IP, the former scenario is preferable; the electron cooling occurred to the center-northwest direction.

The electron cooling may occur by a thermal conduction from cold clouds (Cox et al. 1999; Shelton et al. 1999). In this case, the RP should be prominent in the contact region with cold dense clouds. Filipovic et al. (2005) reported that a dense molecular cloud may be interacting with the

SNR shock at the southwest. However, no hint of interaction such as maser sources is found in the cloud. Furthermore, the position of the molecular cloud is significantly off-set from the RP region (Center-NW). Moreover, we see no hint of a thermal conduction: no temperature decrease toward the molecular clouds. Thus the thermal conduction is unlikely for the RP in the Center to the NW of G290.1–0.8.

We therefore discuss an alternative scenario of the rapid electron cooling, an adiabatic rarefaction (Itoh & Masai 1989; Shimizu et al. 2012). Since the ejecta of RP is aligned from the Center to the NW, and the electron temperature decreases toward the same direction, the rarefaction would be jet-like pointing to the NW. Also the X-ray/radio morphologies of G290.1–0.8 extend further to the NW.

Since the best-fit $n_e t$ and kT_e values may suggest the higher pressure in the RP than that in the IP region, one may argue that this is inconsistent with the rarefaction scenario. However, our rarefaction scenario is not a break-out from the IP (NE and SW) to the RP (Center and NW) regions. We assume that the ejecta became a RP by an adiabatic break-out from the high density circumstellar region (very near the SNR center) to the low density ISM region, while the IP is the result of independent process: canonical ionizing process.

Assuming the distance of 7 kpc and using the best-fit $n_e t$ and EM in the NW region, the recombining time (t_{rec}) is estimated to be $50 (f/0.25)^{0.5} \text{ kyr}$. While this value is larger than the estimated SNR age of 10–20 kyr (Slane et al. 2002), This disagreement is probably due to the simplified age estimation of the complex SNR. In fact, Halpern et al. (2014) reported the spin-down age of the pulsar to be 116 kyr, which favors our recombining time. If the SNR age is equal to the recombining time of $50 (f/0.25)^{0.5} \text{ kyr}$, the kick velocity of the pulsar is $400 (f/0.25)^{-0.5} \text{ km s}^{-1}$. This is consistent with the mean value of pulsars of $450 \pm 90 \text{ km s}^{-1}$ (Lyne & Lorimer 1994), and contradicts the high kick velocity of 1000–2000 km s^{-1} , estimated by Pavan et al. (2014).

Since the long-jet of IGR J11014-6103 is pointing to the northwest, the same direction of the RP region, it may be conceivable that the RP was made by the jet when the pulsar was still in the main body of the SNR. However, this scenario would be a remote possibility because the jet energy is far less to make a significant over-ionization at the NW plasma, unless it was extraordinary bright, like a gamma-ray burst and its afterglow.

5. Summary

We have analyzed Suzaku/XIS data obtained from G290.1–0.8. The results are summarized as follows:

1. The plasma states in G290.1–0.8 are different from region to region. We find Si Ly α and RRCs from the NW and the Center spectra, while not from other regions. Thus the plasmas are in the recombining phase at the Center and the NW, while in the ionizing phase at other regions.
2. The electron temperature of the RP is lower than that of the IP.

3. The abundance pattern indicates that the RP is dominated by ejecta of CC SN, while the IP is likely ISM origin.
4. A plausible origin of the RP is the adiabatic rarefaction to the NW direction.

Acknowledgment

We thank all members of the Suzaku operation and calibration teams. This work is supported by Japan Society for the Promotion of Science (JSPS) KAKENHI Grant Number 23000004, 23340071, 24540229, 24684010, 24740167, 25800119, 26800102.

References

- Abdo, A. A., et al. 2010, *ApJ*, 712, 459
- Anders, E., & Grevesse, N. 1989, *Geochim. Cosmochim. Acta*, 53, 197
- Borkowski, K. J., Hendrick, S. P., & Reynolds, S. P. 2006, *ApJ*, 652, 1259
- Brinkman, A. C., et al. 2000, *ApJL*, 530, L111
- Cox, D. P., Shelton, R. L., Maciejewski, W., Smith, R. K., Plewa, T., Pawl, A., & Różyczka, M. 1999, *ApJ*, 524, 179
- Ergin, T., Sezer, A., Saha, L., Majumdar, P., Chatterjee, A., Bayirli, A., & Ercan, E. N. 2014, *ApJ*, 790, 65
- Filipovic, M. D., Payne, J. L., & Jones, P. A. 2005, *Serbian Astronomical Journal*, 170, 47
- García, F., Combi, J. A., Albacete-Colombo, J. F., Romero, G. E., Bocchino, F., & López-Santiago, J. 2012, *A&A*, 546, A91
- Halpern, J. P., et al. 2014, *ApJL*, 795, L27
- Henley, D. B., & Shelton, R. L. 2013, *ApJ*, 773, 92
- Ishisaki, Y., et al. 2007, *PASJ*, 59, 113
- Itoh, H., & Masai, K. 1989, *MNRAS*, 236, 885
- Jones, T. W., et al. 1998, *PASP*, 110, 125
- Kaneda, H., Makishima, K., Yamauchi, S., Koyama, K., Matsuzaki, K., & Yamasaki, N. Y. 1997, *ApJ*, 491, 638
- Kesteven, M. J., & Caswell, J. L. 1987, *A&A*, 183, 118
- Kesteven, M. J. L. 1968, *Australian Journal of Physics*, 21, 739
- Koyama, K., et al. 2007, *PASJ*, 59, 23
- Kushino, A., Ishisaki, Y., Morita, U., Yamasaki, N. Y., Ishida, M., Ohashi, T., & Ueda, Y. 2002, *PASJ*, 54, 327
- Lyne, A. G., & Lorimer, D. R. 1994, *Nature*, 369, 127
- Miceli, M., Bocchino, F., Decourchelle, A., Ballet, J., & Reale, F. 2010, *A&A*, 514, L2
- Milne, D. K., Caswell, J. L., Kesteven, M. J., Haynes, R. F., & Roger, R. S. 1989, *Proceedings of the Astronomical Society of Australia*, 8, 187
- Mitsuda, K., et al. 2007, *PASJ*, 59, 1
- Nakajima, H., et al. 2008, *PASJ*, 60, 1
- Ohnishi, T., Koyama, K., Tsuru, T. G., Masai, K., Yamaguchi, H., & Ozawa, M. 2011, *PASJ*, 63, 527
- Ohnishi, T., Uchida, H., Tsuru, T. G., Koyama, K., Masai, K., & Sawada, M. 2014, *ApJ*, 784, 74
- Ozawa, M., Koyama, K., Yamaguchi, H., Masai, K., & Tamagawa, T. 2009, *ApJL*, 706, L71
- Pavan, L., Bozzo, E., Pühlhofer, G., Ferrigno, C., Balbo, M., & Walter, R. 2011, *A&A*, 533, A74
- Pavan, L., et al. 2014, *A&A*, 562, A122
- Reynoso, E. M., Johnston, S., Green, A. J., & Koribalski, B. S. 2006, *MNRAS*, 369, 416
- Rho, J., & Petre, R. 1998, *ApJL*, 503, L167
- Sawada, M., & Koyama, K. 2012, *PASJ*, 64, 81
- Serlemitsos, P. J., et al. 2007, *PASJ*, 59, 9
- Seward, F. D. 1990, *ApJS*, 73, 781
- Shelton, R. L., Cox, D. P., Maciejewski, W., Smith, R. K., Plewa, T., Pawl, A., & Różyczka, M. 1999, *ApJ*, 524, 192
- Shimizu, T., Masai, K., & Koyama, K. 2012, *PASJ*, 64, 24

Slane, P., Smith, R. K., Hughes, J. P., & Petre, R. 2002, *ApJ*, 564, 284

Tawa, N., et al. 2008, *PASJ*, 60, 11

Uchida, H., et al. 2012, *PASJ*, 64, 141

Uchiyama, H., Nobukawa, M., Tsuru, T. G., & Koyama, K. 2013, *PASJ*, 65, 19

Woosley, S. E., & Weaver, T. A. 1995, *ApJS*, 101, 181

Yamaguchi, H., Koyama, K., & Uchida, H. 2011, *PASJ*, 63, 837

Yamaguchi, H., Ozawa, M., Koyama, K., Masai, K., Hiraga, J. S., Ozaki, M., & Yonetoku, D. 2009, *ApJL*, 705, L6

Yamauchi, S., Nobukawa, M., Koyama, K., & Yonemori, M. 2013, *PASJ*, 65, 6

Yusef-Zadeh, F., Wardle, M., Rho, J., & Sakano, M. 2003, *ApJ*, 585, 319

Table 1. Observation logs.

	Target	Obs. ID	Obs. Date	(l, b)	Exposure
Source	G290.1–0.8	506061010	2011-Jun-25	$(290^{\circ}1, -0^{\circ}75)$	110.6 ks
Background	1E1048.1–5937	403005010	2008-Nov-30	$(288^{\circ}3, -0^{\circ}52)$	100.4 ks

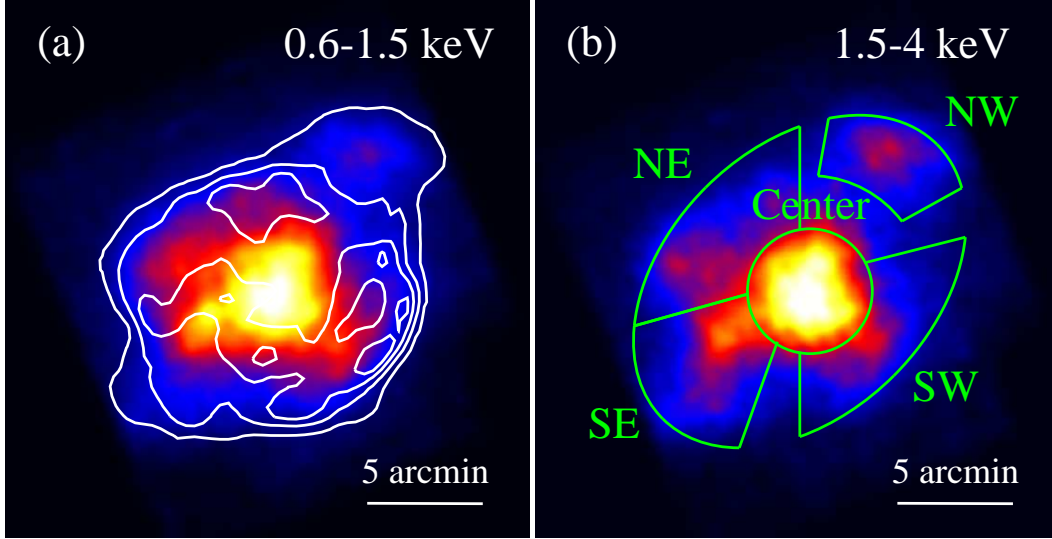


Fig. 1. XIS images of G290.1–0.8 in the energy bands of (a) 0.6–1.5 keV and (b) 1.5–4 keV, respectively. The 843 MHz radio profile is overlaid on (a) with white contours. The spectral extraction regions are shown with the green lines in (b).

Table 2. Best-fit parameters for the background spectrum.

Component	Parameter	Value
Abs1	N_{H} (10^{21}cm^{-2})	13.2 (fixed)
CXB	photon index	1.4 (fixed)
	flux [†]	1.94 (fixed)
Abs2	N_{H} (10^{21}cm^{-2})	7.0 ± 0.8
HP	kT_{e} (keV)	7 (fixed)
	all elements [‡]	< 0.2
LP	kT_{e} (keV)	1 (fixed)
	all elements [‡]	0.10 ± 0.02
Abs3	N_{H} (10^{21}cm^{-2})	4.1 ± 0.7
GH	kT_{e} (keV)	0.16 ± 0.01
	O [‡]	$0.06^{+0.03}_{-0.02}$
	Ne [‡]	0.17 ± 0.02
	Mg [‡]	$0.28^{+0.15}_{-0.14}$
	Others [‡]	1 (fixed)
$\chi^2_{\nu}/\text{d.o.f.}$		1.08/1111

[†] Flux ($10^{-11}\text{erg cm}^{-2}\text{s}^{-1}\text{deg}^{-2}$) in the 2 – 10 keV band.

[‡] Relative to the solar value (Anders & Grevesse 1989).

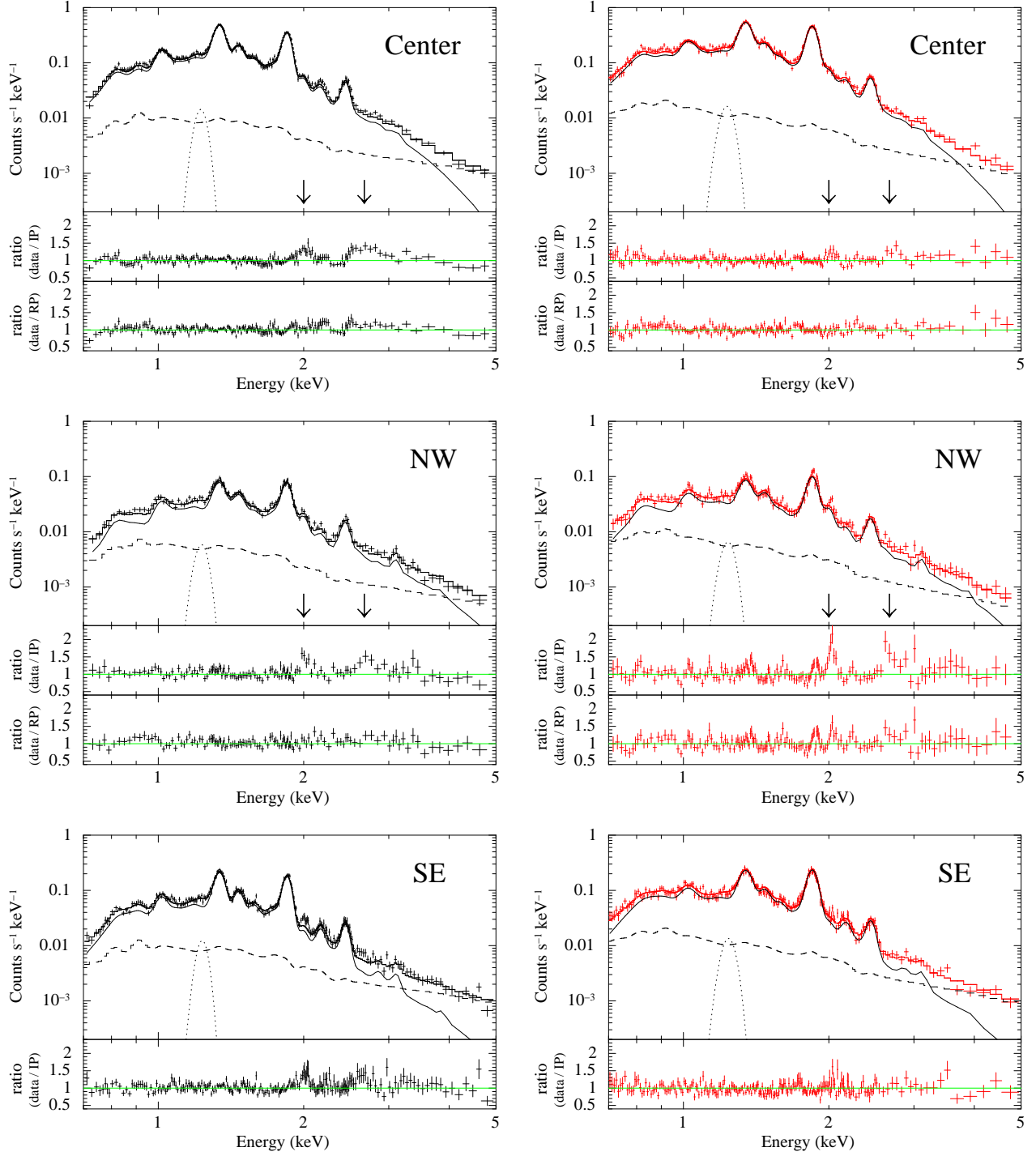


Fig. 2. Spectra obtained from five regions (black: FI, red: BI). Each spectrum is fitted with the plasma model (solid line) + the background model (dashed line) + one Gaussian (dotted line). For the plasma model, the RP is employed in the Center and the NW, while the IP is employed in the SE, NE, and SW. The bottom panels are the ratios of the data to the models we applied. For the Center and the NW, we show the ratios of the data to the IP models in the middle panels for comparison. Error bars represent 1σ confidence levels.

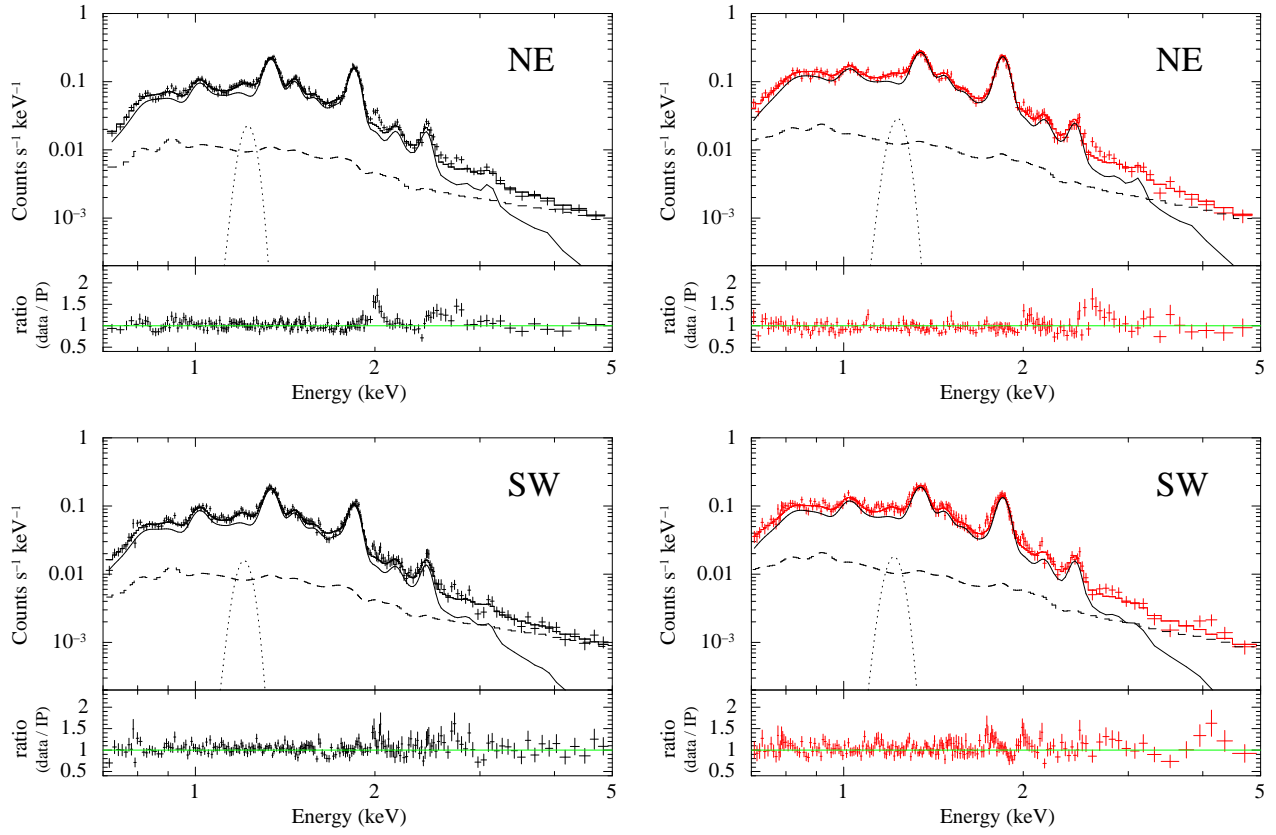


Fig. 2. Continued.

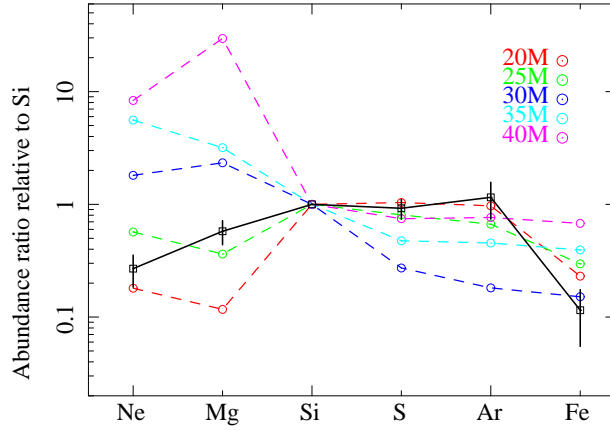


Fig. 3. Abundance pattern of the NW plasma (black solid line). Each elemental abundance is normalized by the value of Si. The red, green, blue, light blue, and magenta dashed lines represent core-collapse models with progenitor masses of 20, 25, 30, 35, and 40 M_{\odot} , respectively (Woosley & Weaver 1995)

Table 3. Best-fit parameters for G290.1–0.8 spectra.

Parameter	Center	NW	SE	NE	SW
	RP	RP	IP	IP	IP
N_{H} (10^{21}cm^{-2})	$7.8^{+0.3}_{-0.5}$	$9.6^{+0.8}_{-1.4}$	$6.8^{+0.7}_{-0.8}$	$6.7^{+0.5}_{-0.6}$	$6.2^{+0.7}_{-0.8}$
kT_{init} (keV)	$1.7^{+1.2}_{-0.3}$	> 1.9	—	—	—
kT_{e} (keV)	$0.45^{+0.02}_{-0.01}$	$0.52^{+0.02}_{-0.04}$	$0.66^{+0.03}_{-0.02}$	$0.64^{+0.02}_{-0.01}$	$0.59^{+0.03}_{-0.02}$
$n_{\text{e}t}$ (10^{12}s cm^{-3})	$1.22^{+0.13}_{-0.09}$	$1.06^{+0.06}_{-0.20}$	$0.34^{+0.07}_{-0.06}$	$0.42^{+0.09}_{-0.07}$	$0.64^{+0.25}_{-0.18}$
EM^{\dagger} (10^{11}cm^{-5})	23^{+2}_{-1}	$4.0^{+0.7}_{-0.5}$	$4.9^{+0.4}_{-0.5}$	5.9 ± 0.4	$4.9^{+0.3}_{-0.5}$
Ne^{\ddagger}	$0.43^{+0.04}_{-0.06}$	0.7 ± 0.2	$0.36^{+0.08}_{-0.07}$	$0.43^{+0.09}_{-0.08}$	0.5 ± 0.1
Mg^{\ddagger}	1.5 ± 0.1	1.5 ± 0.3	1.3 ± 0.1	1.2 ± 0.1	1.2 ± 0.2
Si^{\ddagger}	$2.5^{+0.1}_{-0.2}$	$2.6^{+0.4}_{-0.3}$	$2.0^{+0.2}_{-0.1}$	1.6 ± 0.1	$1.4^{+0.2}_{-0.1}$
S^{\ddagger}	2.1 ± 0.2	$2.4^{+0.4}_{-0.3}$	$1.5^{+0.1}_{-0.2}$	1.1 ± 0.1	$1.1^{+0.1}_{-0.2}$
$\text{Ar}^{\ddagger} (= \text{Ca}^{\ddagger})$	2 ± 1	3 ± 1	$1.1^{+0.7}_{-0.6}$	1.3 ± 0.6	< 1.6
$\text{Fe}^{\ddagger} (= \text{Ni}^{\ddagger})$	$0.10^{+0.02}_{-0.03}$	$0.3^{+0.1}_{-0.2}$	$0.16^{+0.06}_{-0.05}$	0.22 ± 0.05	$0.18^{+0.07}_{-0.06}$
$\chi^2_{\nu}/\text{d.o.f.}$	1.12/1436	1.10/749	1.08/1126	1.06/1198	1.10/1080

[†] Volume emission measure, $\int n_{\text{e}} n_{\text{H}} dV / (4\pi D^2)$, where V and D are the emitting volume (cm^3) and the distance to the source (cm), respectively.

[‡] Relative to the solar value (Anders & Grevesse 1989).